

Dalton Transactions

Accepted Manuscript



This is an *Accepted Manuscript*, which has been through the Royal Society of Chemistry peer review process and has been accepted for publication.

Accepted Manuscripts are published online shortly after acceptance, before technical editing, formatting and proof reading. Using this free service, authors can make their results available to the community, in citable form, before we publish the edited article. We will replace this *Accepted Manuscript* with the edited and formatted *Advance Article* as soon as it is available.

You can find more information about *Accepted Manuscripts* in the [Information for Authors](#).

Please note that technical editing may introduce minor changes to the text and/or graphics, which may alter content. The journal's standard [Terms & Conditions](#) and the [Ethical guidelines](#) still apply. In no event shall the Royal Society of Chemistry be held responsible for any errors or omissions in this *Accepted Manuscript* or any consequences arising from the use of any information it contains.

Hierarchical cupric oxide nanostructures on copper substrate for cold cathode emission: an experimental venture with theoretical correlation

Swati Das¹, Subhajit Saha², Dipayan Sen¹, Uttam Kumar Ghorai², and Kalyan Kumar Chattopadhyay^{1,2*}

¹Department of Physics, Jadavpur University, Kolkata-700032, India

²School of Materials Science and Nanotechnology, Jadavpur University, Kolkata-700032, India

Abstract

In this paper we report a facile route for the synthesis of controlled CuO nano-architectures directly grown on the copper substrate by one step simple chemical route with varying concentration of non-ionic surfactant PEG-6K. The phase purity and degree of crystallinity of the as-developed nanostructures were systemically investigated by X-ray diffraction, X-ray photoelectron spectroscopy and high resolution transmission electron microscopy (HRTEM). A detailed analysis by field emission scanning electron microscopy confirmed the uniformity of the prepared nanostructures over substrates. These architectures displayed substantial improvement of field emission properties with respect to other structures of CuO reported so far. A particular nanostructure (needle) among them showed a down shift of the turn-on field to $2.2 \text{ V}/\mu\text{m}$ coupled with a good enhancement factor (β) ~ 516 , which are deemed as sufficient for electron emission based applications such as field emission displays and vacuum nano-electronic devices. The origin of this efficient field emission from CuO nano-architectures, were probed computationally by investigating the local electric field distribution through finite element based simulation method using ANSYS Maxwell.

Keywords: CuO nanoarchitectures, field emission, electrostatic calculation

Introduction:

Aligned semiconductor nanostructures are presently at the foci of collective research endeavours owing to their unique properties and wide spread applications in the fields of advanced electronic and electromechanical nanodevices [1-3], field emitters, [4] solar cells, [5] sensing, [6-8] drug delivery, [9] magnetic storage media [10] etc. Till now, considerable effort has been devoted to synthesize semiconductor nanostructure arrays via chemical or physical routes in a controlled way. But, the dimensionality requirements, when coupled with the necessary geometry tailoring concerns, constitute one of the major challenges and crucial factor in the progression of nanoscience and nanotechnology. However, it still remains as an active and strongly motivating field of research as the search of suitable methods for growing the tailored nanocrystal such as nanowires, nanoribbons and nanorods and others continues.

In the recent years, the research on cold cathode emitters came in the forefront of micro/nanotechnologies due to their high emission current density at low electric fields and at room temperature along with high emission stability and importantly, no heating of the surrounding device housing. However, the dimensions of nanostructured materials affect the field-emission property profoundly. According to the Fowler-Nordheim (F-N) theory, [11] the field emission of a material is solely dependent on two essential parameters, the work function of an emitting material and the field enhancement factor. The intrinsic work function of inorganic semiconductor generally lies in between 1-7 eV, so lesser the work function better will be the emission efficiency. Secondly, the field-enhancement factor, which is the ratio of the local field to the applied field, depends solely on the shape and morphology of an emitter. Consequently, tailored nanostructures with low work function and sharp geometries are the basic requirement for cold cathode emission. Successful realization of controlled

growth of the nanostructures can open up further wide-ranging opportunities not only in fundamental science but also in potential utilizations in diverse functional devices.

Among the various inorganic semiconductors, nanostructured CuO [12-19] has attracted a much attention because of its wide range of applications, including gas sensing [20-24], field emission, supercapacitor, removal of inorganic pollutants catalyst, photocatalyst, recyclable catalyst, magnetic storage media, super hydrophobic surfaces, etc. [25-31]. Apart from all these wide range of application, in particular, the FE behaviour of nanostructured CuO has been an intense field of research during the past decade due to their thermal stability, large scale production, high aspect ratio, and low work function.

In the current work, we have adopted a simple and versatile approach to grow cupric oxide nanoarchitectures on a metal surface (copper foil) through a simple wet chemical route under ambient condition. In contrast to the heavy equipment and highly expensive physical deposition techniques, the wet chemistry route excels as it is economically most viable and it can operate in low-processing temperatures, with a simple process set-up and within a short time. Additionally, the current synthesis technique uses only non-toxic inorganic salts (sodium hydroxide, ammonia solution) and a bio-compatible organic template (PEG 6K) which is easy to remove only by water rinsing. As a result, the current method is highly effective in exerting precise control over shape, dimensionality, and crystallinity of the desired nanoarchitectures and offers a striking and convenient pathway to the large-scale engineering of ordered inorganic nanostructures on arbitrarily shaped metal electrodes or substrates. In addition, a finite element method based computer simulation was also utilized to theoretically examine the trends of the local electric field on the surface of such morphologies to gain deeper understanding of their field emitting traits.

Experimental Section:

Synthesis: CuO nanoarchitectures were synthesized by in-situ crystallization over the metallic Cu foil. Prior to the growth of nanoarchitectures, copper foils (2×2 cm, Merck, purity: >99.5%, thickness: 0.15 mm) were properly cleaned by ultrasonication in 3 M HNO₃ for 5 minutes and subsequently in absolute ethanol and DI water before use. In next step, the synthesis was carried out in a 100 ml Pyrex glass bottle where 80 ml nutrient solution was prepared by adding 3 ml of 13 M ammonia (28%) solution and 5 ml of 1 M NaOH solution with poly-ethylene glycol (1-4 mM PEG-6K, henceforth, we denote the sample by P1, P2, P3, P4, P5) in DI water. Then the cleaned copper foils were immersed into the solution at a temperature of 30 °C. After 2 days, the foils are taken out from the solution. Furthermore, the samples were washed several times with DI water and ethanol to get rid of the surfactant and hydroxides and dried overnight at 40° C in a vacuum oven. The brown copper foil at this point appeared black which confirmed the formation of cupric oxide on the entire substrate.

CuO nanoarchitectures characterization: The crystallinity and phase purity of the samples were examined by x-ray diffraction (XRD) using Cu K α radiation ($\lambda = 1.5406\text{\AA}$) (Bruker D8 Advanced). High-resolution Raman spectra were obtained with the excitation (λ_{exc}) of 532 nm laser source (WITECH). The morphologies of the prepared products were characterized with field emission scanning electron microscopy (FESEM, S-4800, Hitachi), and high resolution transmission electron microscopy (JEOL, JEM 2100). The chemical state of the constituent elements were examined by X-ray photoelectron spectroscopy using monochromatic Al K α ($h\nu = 1486.6\text{ eV}$) X-ray source and a hemispherical analyzer (SPECS, HSA 3500).

Field Emission Measurement: The field emission measurement of the CuO nanoarchitectures were carried out in a high vacuum (2×10^{-6} mbar) chamber, where a

conical shaped stainless steel electrode served as an anode with a tip diameter ($2R$) of ~ 1.5 mm and the CuO nanoarchitectures on the Cu foil served as the cathode. The cathode was connected with a $1\text{ M}\Omega$ resistor. The separation (d) between the anode and the grounded cathode samples were maintained at a fixed distance ($130\text{ }\mu\text{m}$) during the measurement.

Computational details: For CuO nanoarchitectures based cathodes and stainless steel anodes, calculations of the electric field distribution have been carried out using finite element method. The separation distance between anode-cathode (d) was maintained at $130\text{ }\mu\text{m}$ in direct analogy to the experiment and the radius of the anode used was 1.5 mm . During the calculation, an equipotential negative voltage of -1.9 kV is applied to the cathode, while the anode was maintained at a constant potential value of 0 V . The whole system was maintained inside a vacuum chamber during all steps of the computation process.

2. Results and Discussion:

2.1 Structural and Morphological Characterization:

CuO nanoarchitectures on the Cu foil were grown by a simple, cost effective, one pot wet chemical synthesis method at room temperature. Optical image of as synthesized film grown on Cu foil is shown in Figure S1 (given in ESI). The as synthesized black coloured films with varying concentration of PEG 6K were examined by XRD analysis as shown in Figure 1(a). All the peaks can be clearly indexed to monoclinic phase CuO (space group $C2/c$). A strong diffraction peak from the Cu foil is also detected in the XRD pattern. As compared with the standard diffraction peaks from JCPDS Card No. 05-0661, no other peak is observed belonging to the impurities, such as $\text{Cu}(\text{OH})_2$ or Cu_2O , representing the high purity of as-obtained samples. A magnified image of the XRD pattern of synthesized CuO nanoarchitectures are shown in the right column for better confirmation of the phase purity of the samples. Highly crystalline and slightly broadened diffraction peaks are indexed as

(110), ($\bar{1}11$), (111) respectively. The purity and the composition of the CuO nanoarchitectures were further investigated by X-ray photoelectron spectroscopy. The characteristic survey XPS spectrum of P3 sample is shown in Figure S2 (shown in ESI). The binding energies obtained in the XPS analysis were revised by charge correction of C 1s peak at 284.6 eV which appeared due to the presence of adventitious carbon on the surface of the samples during atmospheric exposure. In the characteristic high resolution XPS spectrum (shown in figure 1(b)), Cu 2p_{3/2} and Cu 2p_{1/2} peaks were centred at 933.65 and 953.5 eV with the splitting of 19.9 eV [32]. Moreover, the two extra shake-up satellite peaks along with the main peaks were also observed at 943.36 eV and 962.37 eV which indicates the presence of an unfilled Cu 3d⁹ shell and thus further confirmed the presence of the Cu²⁺ chemical state as an indication of the formation of CuO [33]. High resolution core level spectra of O 1s state (shown in figure 1(b) below the Cu²⁺ HR spectra) shows a broad asymmetric curve which was fitted into two Gaussian peaks by standard curve fitting procedure using CASA XPS software. The distinctive peak is attributed to O²⁻ bonded with Cu²⁺ at 529.9 eV and the second peak at 531.31 eV suggests surface adsorbed oxygen on CuO nanoarchitectures. The above results are in well accordance with the previous literature reports [34] and also support the finding from XRD data.

Raman spectroscopy is also broadly applied to investigate the structural properties of nanoscale materials as it sensitively probes the local atomic arrangements and vibrations of the materials. Monoclinic CuO belongs to the space group of the C_{2h}⁶ which has 12 phonon branches for their four atoms in the primitive cell. From factor-group analysis, zone center modes are as follows:

$$\Gamma_{\text{vibrational}} = A_g + 2B_g + 4A_u + 5B_u$$

Amongst the nine optical modes, three ($A_g + 2B_g$) are Raman-active, and the remaining six ($3A_u + 3B_u$) are IR-active [35]. In figure 1(c) three Raman peaks for all CuO nanoarchitectures at 288, 330, and 621 cm^{-1} are observed. The peak at 288 cm^{-1} is allocated to the A_g mode and the peaks at 330 and 621 cm^{-1} correspond to the B_g modes. The results are in good agreement with the previously reported values. The entire range of Raman spectrum from 200-2900 cm^{-1} is presented in the figure S3 in ESI.

Further, morphology and structures of the produced CuO nanoarchitectures were checked using field emission scanning electron microscopy (FESEM) as shown in Figure 2(a₁)-(d₁). The low-magnification FESEM images show the network of CuO nanostructures, distributed uniformly and compactly over the entire surface of the copper foil. Categorically, we can see that the images in figure 2(a₁-d₁) visualize the macroscopic formation of cauliflower like unique shape with the assembly of individual nanostructures. The high-magnification FESEM images (beneath) illustrate the morphologies and alignments of individual nanostructures. It contains numerous nano-architectures with different geometry depending on the synthesis condition. The synthesis condition is tabulated in detail in table1. The surface morphology of the Sample P1 (Figure 2a₂) is a network of CuO nanoplates oriented in an arching fashion to the surface of substrate. The average length and breadth of these nanoplates are observed to be ~250-300 nm and ~150 nm, respectively, whereas the thickness is approximately 100 nm. A closer look shows that the flakes further split at the end into filament or ribbon like nanostructures. Intense Brownian motion of the surfactant molecules can influence this type of crystal splitting [32]. Afterward, a careful observation of Sample P2 (Figure 2b₂) shows the dense and compact flower like nanostructure arranged over a macroscopic range. The magnified image reveals petal like nanostructure which contains numerous flexible and highly transparent edges with a mean thickness lesser than 5-8 nm and a length of 400-500 nm. In Figure 2c₂ the morphology is different as change of concentration

of the surfactant modulated the entire nanostructure. This image depicts the highly dense 1D CuO nanoneedle of tip diameter $\sim 6-8$ nm and length of 300-400 nm, oriented almost perpendicular to the substrate. These nanostructures are connected to each other through their wider bases and are rooted in a common center to form a flower-like morphology. Figure 2d₂ displays a diverse registry of the nanostructures distributed hemi-spherically on the substrate. The capping agent, PEG 6K restricts the passivation of ions to the substrate, thus a knife patterned nanostructures are formed. The nanoknives have well defined sharp side edges with a pinning tip and are rooted in a broader base. The sharp tip end is around 7-10 nm in diameter and $\sim 250-300$ nm in length. An inset of Figure 2(a₂-d₂) shows the magnified micrograph of each individual nanostructures. Further increase in the soft template concentration (sample P5) does not show any drastic change in morphology but mostly display the same flaky pattern with a bigger nanostructure (as shown in Figure S4).

To investigate the interior structures of the as-grown CuO architectures in detail, further TEM analyses were also conducted. Figure 2(a₃- d₃) are bright-field TEM images of obtained CuO architectures, along with their individual nanostructures. Interestingly, the TEM micrograph reveals that rough surface structures are composed of a few hundreds of small well-aligned nano crystals self-assembled into hierarchical architecture.

The EDAX pattern demonstrates that the products are made of Cu and O only and the atomic ratio of Cu to O is $\sim 1:1$ for all nanostructures shown in Figure 3(b). Further, elemental mapping obtained from EDAX of sample P4 in figure 3(a) confirms that Cu and O are uniformly distributed throughout the synthesized nanostructures as represented in figure 3(c, d). In addition, HRTEM image of a single nanoknife circled in figure 3(e) demonstrate that the measured interplaner spacing of the lattice fringe is 2.35 Å, which corresponds well to the [111] crystallographic planes of monoclinic CuO. Uniform and well resolved lattice fringes

also reflect the well crystalline nature of the nanostructures. Its SEAD pattern confirms that the CuO nanostructures are polycrystalline in nature (shown in Figure S5 of ESI). The CuO nanostructures are found to be very stable even after the high energy e-beam irradiation during the HRTEM characterization.

Growth mechanism:

Controlled synthesis and in situ tailoring of the morphology and dimensionality of nanostructure assemblies are currently at the focus of attention of the research community. Experimental parameters such as reaction temperature, reactant concentration, surfactants and most importantly the pH value of the precursor plays a significant role in morphological and microstructural control of nanocrystals. pH tunable nanostructures have been extensively studied on the basis of the fact that the concentration of OH^- significantly affect the nucleation and growth of the nanocrystals. At the same time, the addition of ammonia as alkaline reactor plays two major roles: firstly, it controls the basicity of the solution and secondly, it coordinates with Cu^{2+} and give rise to a $\text{Cu}(\text{NH}_3)_4^{2+}$ complex. At high pH (11.5), high concentration of $\text{Cu}(\text{NH}_3)_4^{2+}$ complex further transforms into square planner complex of $\text{Cu}(\text{OH})_2$. These blue colored $\text{Cu}(\text{OH})_2$ exists momentarily and after that decomposes into 1D CuO nanocrystals. In this study, electron microscopy has revealed that the final nanostructures are consisted of nanosized crystals (illustrated in figure 4). Thus, it's evident that they originate from the original small crystallites by the process of "oriented attachment" followed by the arrangement along identical crystal faces.

As the pH of the solution was kept fixed at 11.5, formations of different type of nanostructures can be solely attributed to the effect of soft templates. PEG is a polymer that has a chain like structure $[\text{H}-(\text{O}-\text{CH}_2-\text{CH}_2)_n-\text{OH}]$ in water and it serves as the structure directing reagent. Due to the presence of existing large quantity of activated oxygen in PEG

molecular chains, they acted as a network forming agent around the metal ions [19]. Thus, in the reaction process, PEG molecules get adsorbed on $\text{Cu}(\text{OH})_2$ by H bonding to form Cu-PEG units [31] to minimize their surface energy. The prolonged reaction time as well as the reaction temperature decomposes these Cu-PEG units and the CuO nanocrystals (NC) appear. Then the free PEG chains in the solution selectively adsorb on certain faces of the re-emerging CuO nanocrystallites and suppress their intrinsic growth; consequently regular nanostructures are formed. In brief, PEG moderates the effective surface supersaturation and retards diffusion rate so that the reaction process sterically stabilizes the precipitated particles against aggregation. As a result, CuO NC re-emerges in a regular array and individual nanostructures assemble shoulder to shoulder in various orientations to form particular nanostructures. When the initial PEG concentration is only 1 mM, they get adsorbed on a specific plane and the passivation of CuO NC on the other planes remain largely intact; resulting in appearance of thick nanoplates for longer reaction time. With the increase of PEG 6K concentration to 1.5 mM, the non-ionic chain gets arranged in a preferred network via oriented attachment growth which results the formation of needle like nanostructures. Further increase of PEG 6K concentration, results in a different patterned network because PEG 6K retards diffusion and their steric interaction stabilizes the preferred arrangement which further follows a specific oriented growth direction [36]. This assembly of polymeric chain emerges a new form of knife like patterned nanostructures. The schematic illustrates the plausible growth process of the synthesized CuO nanostructures at different concentration of PEG 6K into the solute, which is shown in figure 4. In the proposed scheme, the entire growth process consisted of several stages: At first, formation of $\text{Cu}(\text{NH}_3)_4^{2+}$ takes place and then this complex transforms into $\text{Cu}(\text{OH})_2$. In next step, the homogeneous emulsion of PEG 6K in solute get attached to Cu^{2+} nuclei. Further, Cu-PEG transformed into CuO nanoparticles at room temperature which serves as building block. At the final stage, the building block

further assembled to form the hierarchically organized different nanostructures by the assistance of polymeric network.

Field-emission (FE) measurement:

Field-emission (FE) measurements show that the CuO nanoarchitectures, as shown in table 2, are potentially good field emitters while comparing with the previous reports regarding similar systems. As the growth of these CuO nanostructures is uniform over the top as well as the bottom faces of the copper foil, it restricts the conduction of electrons in our measurement system. For such a reason, the films were properly masked before they were immersed into the reactant solution and were cleaned properly with diluted HCl prior to the FE measurement. The variations of the emission current density with the applied field (J-E) from four different nanostructures are shown in Figure 5. The quasi-aligned nanowire arrays (sample P3) have the best field emission properties with the lowest turn-on field (defined as; E at which J becomes $10 \mu\text{A}/\text{cm}^2$) of $2.2 \text{ V}/\mu\text{m}$, the lowest threshold field (defined as; E at which J becomes $0.1 \text{ mA}/\text{cm}^2$) of $6.8 \text{ V}/\mu\text{m}$, and the highest J at the same E value. The FE current density attains $1.77 \text{ mA}/\text{cm}^2$ when an applied macroscopic field is $14.3 \text{ V}/\mu\text{m}$. Meanwhile, the turn-on fields from the other samples are 2.6 (P4), 2.83 (P2), and 3.7 (P1) $\text{V}/\mu\text{m}$, as shown in Table 1. Sample P4 shows the second highest value among the other nanostructures. Structures with a higher aspect ratio were found to show stronger field emissions. The variation of $\ln(J/E^2)$ with $(1/E)$ (F-N plot) (Figure 5b) implies nonlinear behaviour over the whole range of the applied field, signifying the semiconducting nature of the emitter. At low applied field, the contribution of the emitting electrons arises mainly from the conduction band, whereas with the increase in the applied field, the valence band electrons also tunnel out and contribute in the emission current [37, 38]. The observed variation of morphology dependent field emission property can be well understood on the

basis of band structure of the corresponding materials. The electrons are initially bound by the surface potential energy barrier and the potential energy of the cold cathode can be written as:

$$U(x) = -\frac{e^2}{4x} - \beta eEx + E_F + \varphi \quad (1)$$

Where e is the charge of an electron, x is the distance from the emitter surface, E_F is the Fermi energy level of the cathode materials, φ is the surface potential barrier for the electron, and E is the electric field strength directly on the emitter surface. β is introduced to describe the geometric effect of the micro roughness due to the nanostructural assembly of cold cathode materials on the electric field. A sharp tip can lessen the potential barrier significantly as compared to a flat emitter.

The FE current-voltage characteristics are further analyzed by the Fowler-Nordheim (F-N) equation

$$J = \left(\frac{A\beta^2 E^2}{\varphi}\right) \exp\left(-B \frac{\varphi^{3/2}}{\beta E}\right)$$

$$\text{Or } \ln(J / E^2) = \ln\left(\frac{A\beta^2}{\varphi}\right) - B \frac{\varphi^{3/2}}{\beta E} \quad (2)$$

where A and B are constants with values of $1.54 \times 10^{-6} \text{ eV AV}^{-2}$ and $6.83 \times 10^3 \text{ V}\mu\text{m}^{-1} \text{ eV}^{-3/2}$, respectively, $E = \beta E_0$ is the local electrical field, E_0 is the mean field between the cathode and anode, β is the field enhancement factor and φ is the work function of the emitting materials, which is 4.5 eV for CuO [16]. The field enhancement factor (β) is an important parameter in describing field emission. The enhancement factor β can be calculated from the slope (m) of

the F-N plot of equation (2) at an inter electrode distance of 130 μm from the equation below [39]:

$$\beta = \frac{B\phi^{3/2}d}{\text{slope}} \quad (3)$$

Generally, β values are related to the emitter geometry (such as aspect ratio), crystal structure, vacuum gaps, and the spatial distribution of emitting centres [40]. The calculated field-enhancement factors from the F-N plots are also abridged in Table 2. Quasi-aligned nanoneedle arrays (sample P3) have shown the highest enhancement factor (516) with the lowest value of slope as compared to sample P1 (362), sample P2 (431) and sample P4 (442). The excellent field-emission properties of sample P3 can be attributed to the higher aspect ratio and the better alignment of the structures than those of the other samples.

The high field-enhancement and low turn-on field values indicate that the present nanostructures possess excellent field-emission characteristics. We conclude that high aspect ratio, good crystallinity and special geometry are the principal contributors in this improvement of field-emission characteristics. The choice of substrate is also important in FE as the electron before emission from the nano-tips must have to pass through the junction between substrate and base of the nanostructures. The electrons encounter an energy obstacle at the metal-semiconductor junction due to the band bending at the substrate nanostructure interface. As the metallic copper foil and copper oxide have work functions of 4.53–5.10 eV [41] and 4.5 eV respectively; the electrons must overcome only 0.57 eV energy barriers before ejection. As a consequence copper foil served as a good substrate in case of CuO nanostructures than other substrates like bare Si.

Stability of the field emitters is one of the important parameter related to potential applications. FE stability measurements were performed on nanoneedle arrays (sample P3) by

keeping an electric field at 14 V/ μm over a period of 2 h. As shown in Figure 5c, there were very feeble fluctuations around $\sim 7\%$ during this period. This good emission stability demonstrates that the synthesized CuO nanostructures are having potential applications in the cold-cathode-based electronics.

Computer simulations of the electric field distribution for CuO nanoarchitectures:

To further investigate the origin of this efficient field emission of CuO nano architectures, we computationally investigated the local electric field profile by finite displacement method using ANSYS Maxwell simulation package. To achieve this end, simulation parameters are chosen in a way to reciprocate the experimentally measured dimensions from the TEM images. Simulated results provide accurate insight regarding the effect of nanoscale geometry on local field and screening effect which is otherwise difficult to speculate [46]. Simulated profiles of electric field vector's magnitude for CuO nanoarchitectures (P1, P2, P3, P4) are shown in figure 6. It is seen that the highest field enhancement is achieved for sample P3 (quasi aligned nanoneedle arrays) whereas P4 showed the second highest and the lowest value is shown by P1. A rainbow coloured scale bar is used to map the different electric field intensities on the 3D plane. It is evident from the figure that the local electric field is predominately concentrated on the top of the sharp tips and the edges shows the lowest field distribution. Despite their (sample P3 & P4) close aspect ratio, the densely spaced nanoknife like structures (P4) shows a reduction in the overall local field. The screening effect due to the densely spaced nanostructures might be responsible for the overall decrease in field intensity. Whereas P3 (nanoneedles), due to its quasi aligned arrangement prevents the screening effect and shows enhanced the field emission current density. As a result, the more efficient field emission from the three-dimensional quasi aligned CuO nanoneedles arrays can be recognized to the reduction of the screening effect. The maximum local field for P3 is

found to be $\sim 4.08 \times 10^7$ V/m (F_1) and for sample P4, F_2 become 3.39×10^7 V/m. The field emission enhancement factors β_1 and β_2 for nanoneedle and nanoknife structures can be calculated as $\beta_1 = F_1/F_M$ and $\beta_2 = F_2/F_M$ (F_M = applied macroscopic field) and consequently their ratio simply comes out to be as: $\frac{\beta_1}{\beta_2} = \frac{F_1}{F_2} = 1.2$ which is pretty close to the experimentally obtained value of 1.17.

Conclusion:

We successfully designed a synthesis protocol for large scale growth of CuO nanoarchitectures on copper foil in the presence of non-ionic surfactant PEG at room temperature. The evolution of the structures with change of PEG concentration is studied in detail, and a possible growth mechanism is proposed. Benefit of such anisotropic structures is analysed from their FE performances. As a direct consequence of high aspect ratio and well alignment, CuO nanoneedles display better FE performance with a down shift of turn-on field to 2.2 V/ μm and improved enhancement factor ($\beta \sim 516$). By calculating the electrostatic field distribution, it is found that among all nanostructures, the electrostatic field around the tip of CuO nanoneedles are much higher which reduces the surface potential barrier significantly. Moreover, their flower like patterns diminishes the screening effect considerably. These results strongly suggest the viability of CuO nanoneedles as a competitive cold cathode material in FE microelectronic devices.

NOTE AND REFERENCES:

[†]Electronic Supporting Information Available: digital image of as deposited CuO films on Cu foil, survey spectra of both the thin films obtained from XPS, FESEM image of P5 sample, SEAD pattern polycrystalline CuO nanostructures.

Corresponding Author

*Kalyan Kumar Chattopadhyay: email: kalyan_chattopadhyay@yahoo.com

Tel.:+91 9433389445; Fax: +91 33 2414 6007

ACKNOWLEDGEMENTS

The authors (SD, SS & UKG) would like to thank and acknowledge the financial support from the Council of Scientific and Industrial Research (CSIR), the Government of India, for awarding Senior Research Fellowships during the execution of the work. One of us (DS) wishes to thank the W.B. State Govt. for providing fellowships during the execution of this work. We also wish to thank the Department of Science & Technology (DST) of the Government of India, University Grants Commission for 'University with Potential for Excellence scheme (UPE-II)' and TEQIP programme for financial help.

References:

1. J. Jie, W. Zhang, I. Bello, C.-S. Lee and S.-T. Lee, *Nano Today*, 2010, **5**, 313-336.
2. T. Zhai, L. Li, Y. Ma, M. Liao, X. Wang, X. Fang, J. Yao, Y. Bando and D. Golberg, *Chemical Society reviews*, 2011, **40**, 2986-3004.
3. L. Li, R. Ma, N. Iyi, Y. Ebina, K. Takada and T. Sasaki, *Chemical communications*, 2006, 3125-3127.
4. X. Fang, Y. Bando, U. K. Gautam, C. Ye and D. Golberg, *Journal of Materials Chemistry*, 2008, **18**, 509.
5. J. Xu and D. Xue, *The Journal of Physical Chemistry B*, 2005, **109**, 17157-17161.
6. H. Zhang, Q. Zhu, Y. Zhang, Y. Wang, L. Zhao and B. Yu, *Advanced Functional Materials*, 2007, **17**, 2766-2771.
7. K. J. Choi and H. W. Jang, *Sensors*, 2010, **10**, 4083-4099.
8. M. M. Rahman, A. J. Ahammad, J. H. Jin, S. J. Ahn and J. J. Lee, *Sensors*, 2010, **10**, 4855-4886.

9. M.-Y. Ma, Y.-J. Zhu, L. Li and S.-W. Cao, *Journal of Materials Chemistry*, 2008, **18**, 2722.
10. R. V. Kumar, Y. Diamant and A. Gedanken, *Chemistry of Materials*, 2000, **12**, 2301-2305.
11. R. H. Fowler and L. Nordheim, *Proceedings of the Royal Society A: Mathematical, Physical and Engineering Sciences*, 1928, **119**, 173-181.
12. S. Jana, S. Das, N. S. Das and K. K. Chattopadhyay, *Materials Research Bulletin*, 2010, **45**, 693-698.
13. J. Chen, N. Y. Huang, S. Z. Deng, J. C. She, N. S. Xu, W. Zhang, X. Wen and S. Yang, *Applied Physics Letters*, 2005, **86**, 151107.
14. R. Z. Zhan, J. Chen, S. Z. Deng and N. S. Xu, *Journal of Vacuum Science & Technology B: Microelectronics and Nanometer Structures*, 2010, **28**, 558.
15. D. Shang, K. Yu, Y. Zhang, J. Xu, J. Wu, Y. e. Xu, L. Li and Z. Zhu, *Applied Surface Science*, 2009, **255**, 4093-4096.
16. J. Xu, K. Yu, J. Wu, D. Shang, L. Li, Y. e. Xu and Z. Zhu, *Journal of Physics D: Applied Physics*, 2009, **42**, 075417.
17. S. Das, S. Maiti, S. Saha, N. S. Das and K. K. Chattopadhyay, *Journal of nanoscience and nanotechnology*, 2013, **13**, 2722-2728.
18. H. Wu, D. Lin and W. Pan, *Applied Physics Letters*, 2006, **89**, 133125.
19. S. Das, S. Saha, D. Sen, U. K. Ghorai, D. Banerjee and K. K. Chattopadhyay, *Journal of Materials Chemistry C*, 2014, **2**, 1321.
20. R. K. Bedi and I. Singh, *ACS applied materials & interfaces*, 2010, **2**, 1361-1368.
21. M. Hübner, C. E. Simion, A. Tomescu-Stănoiu, S. Pokhrel, N. Bârsan and U. Weimar, *Sensors and Actuators B: Chemical*, 2011, **153**, 347-353.

22. C. Yuan, Y. Xu, Y. Deng, N. Jiang, N. He and L. Dai, *Nanotechnology*, 2010, **21**, 415501.
23. X. Zhang, G. Wang, W. Zhang, N. Hu, H. Wu and B. Fang, *The Journal of Physical Chemistry C*, 2008, **112**, 8856-8862.
24. O. Akhavan and E. Ghaderi, *Journal of Materials Chemistry*, 2011, **21**, 12935.
25. Y. W. Zhu, T. Yu, F. C. Cheong, X. J. Xu, C. T. Lim, V. B. C. Tan, J. T. L. Thong and C. H. Sow, *Nanotechnology*, 2005, **16**, 88-92.
26. X. Zhang, W. Shi, J. Zhu, D. J. Kharistal, W. Zhao, B. S. Lalia, H. H. Hng and Q. Yan, *ACS nano*, 2011, **5**, 2013-2019.
27. (a) X-Y Yu, R-X Xu, C Gao, T Luo, Y Jia, J-H Liu, *ACS Appl Mater Interfaces* 2012; **4**, 1954–62, (b) I. Ali, *Chemical reviews*, 2012, **112**, 5073-5091.
28. J. Liu, J. Jin, Z. Deng, S. Z. Huang, Z. Y. Hu, L. Wang, C. Wang, L. H. Chen, Y. Li, G. Van Tendeloo and B. L. Su, *Journal of colloid and interface science*, 2012, **384**, 1-9.
29. M. Basu, A. K. Sinha, M. Pradhan, S. Sarkar, A. Pal and T. Pal, *Chemical communications*, 2010, **46**, 8785-8787.
30. C. Rossi, K. Zhang, D. Esteve, P. Alphonse, P. Tailhades and C. Vahlas, *Microelectromechanical Systems, Journal of*, 2007, **16**, 919-931.
31. F. Mumm, A. T. van Helvoort and P. Sikorski, *Acs Nano*, 2009, **3**, 2647-2652.
32. X. Wang, G. Xi, S. Xiong, Y. Liu, B. Xi, W. Yu and Y. Qian, *Crystal growth & design*, 2007, **7**, 930-934.
33. M. Yin, C.-K. Wu, Y. Lou, C. Burda, J. T. Koberstein, Y. Zhu and S. O'Brien, *Journal of the American Chemical Society*, 2005, **127**, 9506-9511.
34. Q. Zhang, K. Zhang, D. Xu, G. Yang, H. Huang, F. Nie, C. Liu and S. Yang, *Progress in Materials Science*, 2014, **60**, 208-337.

35. L. Debbichi, M. C. Marco de Lucas, J. F. Pierson and P. Krüger, *The Journal of Physical Chemistry C*, 2012, **116**, 10232-10237.
36. Q. Zhang, K. Zhang, D. Xu, G. Yang, H. Huang, F. Nie, C. Liu, S. Yang, *Progress in Materials Science*, 2014, **60**, 208–337
37. A. Al-Tabbakh, M. A. More, D. S. Joag, I. S. Mulla and V. K. Pillai, *ACS nano*, 2010, **4**, 5585-5590.
38. S. S. Warule, N. S. Chaudhari, J. D. Ambekar, B. B. Kale and M. A. More, *ACS applied materials & interfaces*, 2011, **3**, 3454-3462.
39. H. W. Kang, J. Yeo, J. O. Hwang, S. Hong, P. Lee, S. Y. Han, J. H. Lee, Y. S. Rho, S. O. Kim, S. H. Ko and H. J. Sung, *The Journal of Physical Chemistry C*, 2011, **115**, 11435-11441.
40. U. K. Gautam, X. Fang, Y. Bando, J. Zhan and D. Golberg, *ACS nano*, 2008, **2**, 1015-1021.
41. CRC Handbook of Chemistry and Physics, 91st ed.; Internet Version 2011.
<http://www.hbcpnetbase.com/>.
42. H.-H. Lin, *Journal of Applied Physics*, 2004, **95**, 5889.
43. L. Yu, G. Zhang, Y. Wu, X. Bai and D. Guo, *Journal of Crystal Growth*, 2008, **310**, 3125-3130.
44. Y. W. Zhu, A. M. Moo, T. Yu, X. J. Xu, X. Y. Gao, Y. J. Liu, C. T. Lim, Z. X. Shen, C. K. Ong, A. T. S. Wee, J. T. L. Thong and C. H. Sow, *Chemical Physics Letters*, 2006, **419**, 458-463.
45. C.-T. Hsieh, J.-M. Chen, H.-H. Lin and H.-C. Shih, *Applied Physics Letters*, 2003, **82**, 3316.
46. U. Ghorai, S. Das, S. Saha, N. Mazumder, . Sen, and K. K. Chattopadhyay; *Dalton Transactions*. 2013, **42**, 12965

Figure caption:

Fig. 1: (a) Representative XRD pattern of CuO nanoarchitectures grown on Cu foil at different concentration and right side of the panel showed magnified image of the XRD pattern for better confirmation of the phase purity of the synthesized samples, (b) High resolution XPS spectra of Cu 2p_{3/2} and Cu 2p_{1/2} core levels and (c) O 1s core level of CuO nanoarchitectures, (c) Experimental Raman spectra of CuO showing Raman active vibrational modes.

Fig. 2: (a₁-d₁) FESEM images of CuO nanoarchitectures grown on Cu foil under different magnifications. 2(a₂-d₂) high magnification image of the above structure and the inset image is showing individual architects. Fig. 2(a₃-d₃) high- magnification TEM images of above nanoarchitectures.

Fig. 3: (a-d) FESEM images along with the EDX elemental mapping of CuO nanostructures (sample P4). (f) HRTEM image of a single assembled nanoknife circled in (e).

Fig. 4: illustration of possible growth mechanism of hierarchically organized microstructure formation by self-assembly of nucleated nanocrystallites.

Fig. 5: (a) Graphical representation of field emission current density versus electric field (J-E) of CuO nanostructured arrays of P1, P2, P3, P4 samples and (b) the corresponding Fowler–Nordheim (FN) plots of the above nanostructures (c) The field emission current stability of the CuO nanoneedle structures over the long period of time.

Fig. 6: Calculated electric-field distributions of all the CuO nanostructures with distinct colour mapping for different magnitude of electric field vectors. The colour scale bar for different electric field intensity are shown for better comparison of the simulated results.

Table 1: Summary of synthesis procedures with the morphological variations of the as-grown CuO nanostructures on copper foil

<i>Sample</i>	<i>Basic solution</i> [NaOH(.1M),NH ₄ OH(.01M)]	<i>Conc. of</i> <i>PEG 6K</i>	<i>Observed product</i> <i>morphology</i>	<i>Turn on</i> <i>(V/μm)</i> <i>at 10μA/Cm²</i>	β
P1	Do	1 mM	Nanoplates	3.7	362
P2	Do	1.5 mM	Nanopetal	2.83	431
P3	Do	2 mM	Nanoneedle	2.2	516
P4	Do	3 mM	Nanoknife	2.6	442
P5	Do	3.5 mM	Nanoknife	3.9	343

Table 2: comparisons of FE result available in the previous literatures:

Method	Type of CuO Nanostructure	Substrate	Turn-on field (V μm⁻¹)	Current density (mA Cm⁻²)	Ref.
Chemical synthesis	Nanoflake, Nanoneedle, Nanoflower	Cu	6, 7, 11.3 (10 μACm ⁻²)	-	12
Chemical synthesis	Straw-like	Cu	3 (0.1 μACm ⁻²)	0.38	26
Electrochemical deposition	Honeycomb	Cu	6-7 (10 μACm ⁻²)	2.5	27
Direct heating on air	Nanowire	Cu	3.5-4.5(10μACm ⁻²)	0.45	25
Gas solid reaction	Nanofibrils	Cu	6 (10 μACm ⁻²)	3	42
Chemical synthesis	Nanoflower	Cu	8.5	-	43
CF₄ plasma treated	Nanowires	Cu	3 (0.1mAcm ⁻²)	1	44
Self-catalytic	Nanofibers	Cu	6-7(10 μACm ⁻²)	2.7	45
Wet chemical synthesis	<u>Nanoneedles (P3)</u>	Cu	2.2(10 μACm ⁻²)	1.77 mA/cm ²	Present work

Figures:

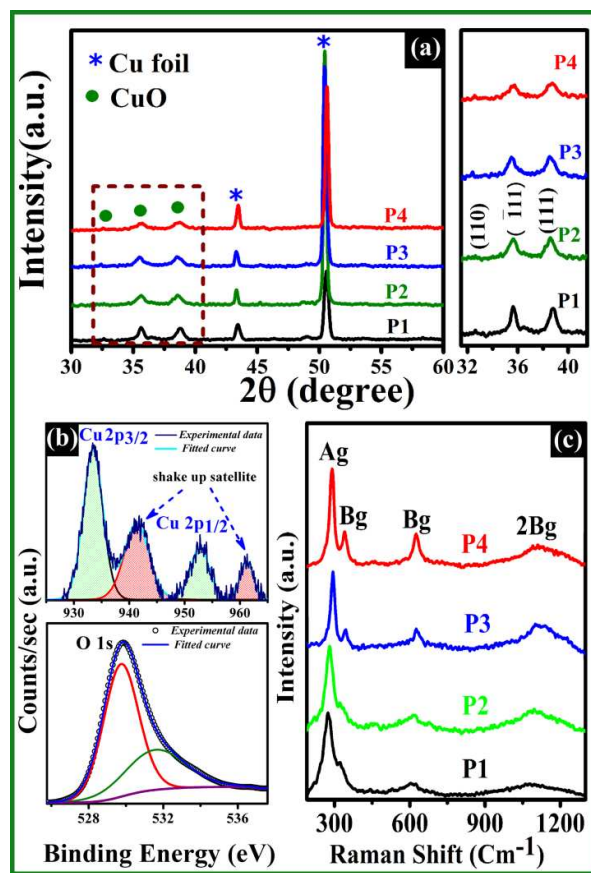


Fig.1

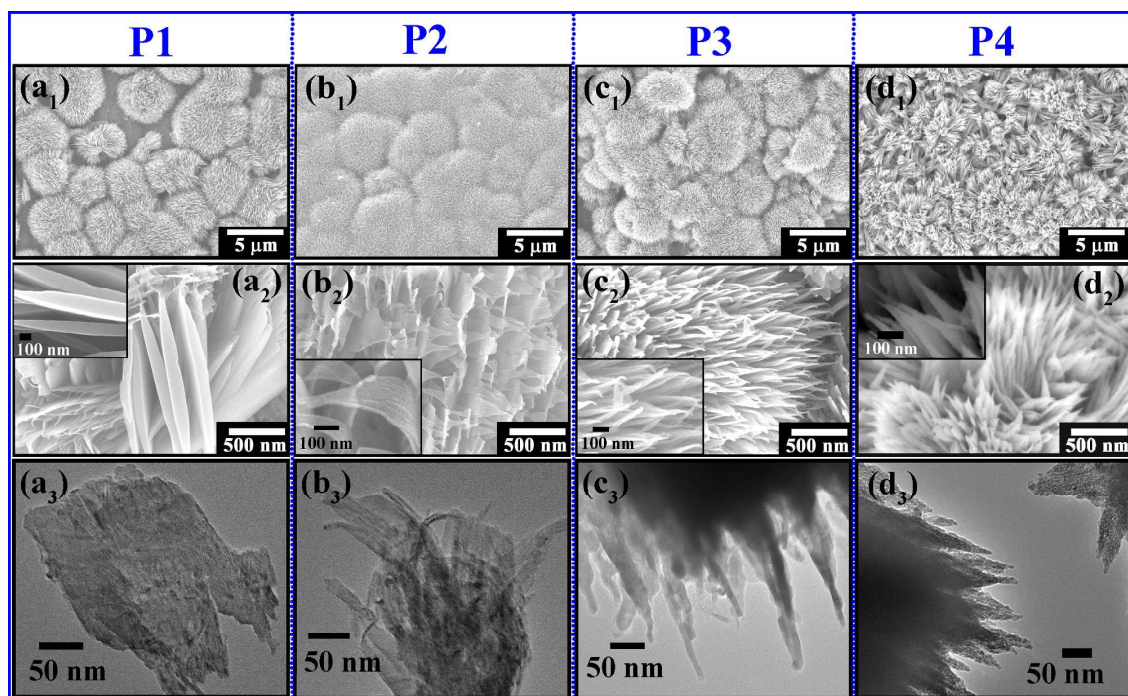


Fig. 2

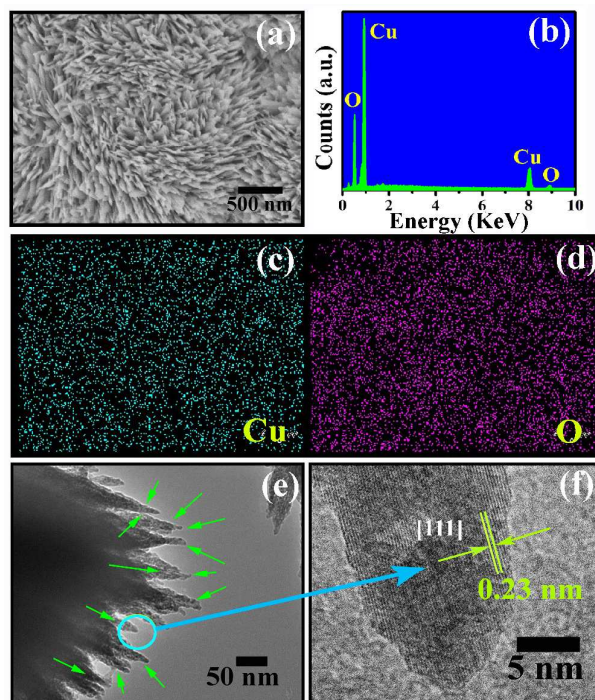


Fig. 3

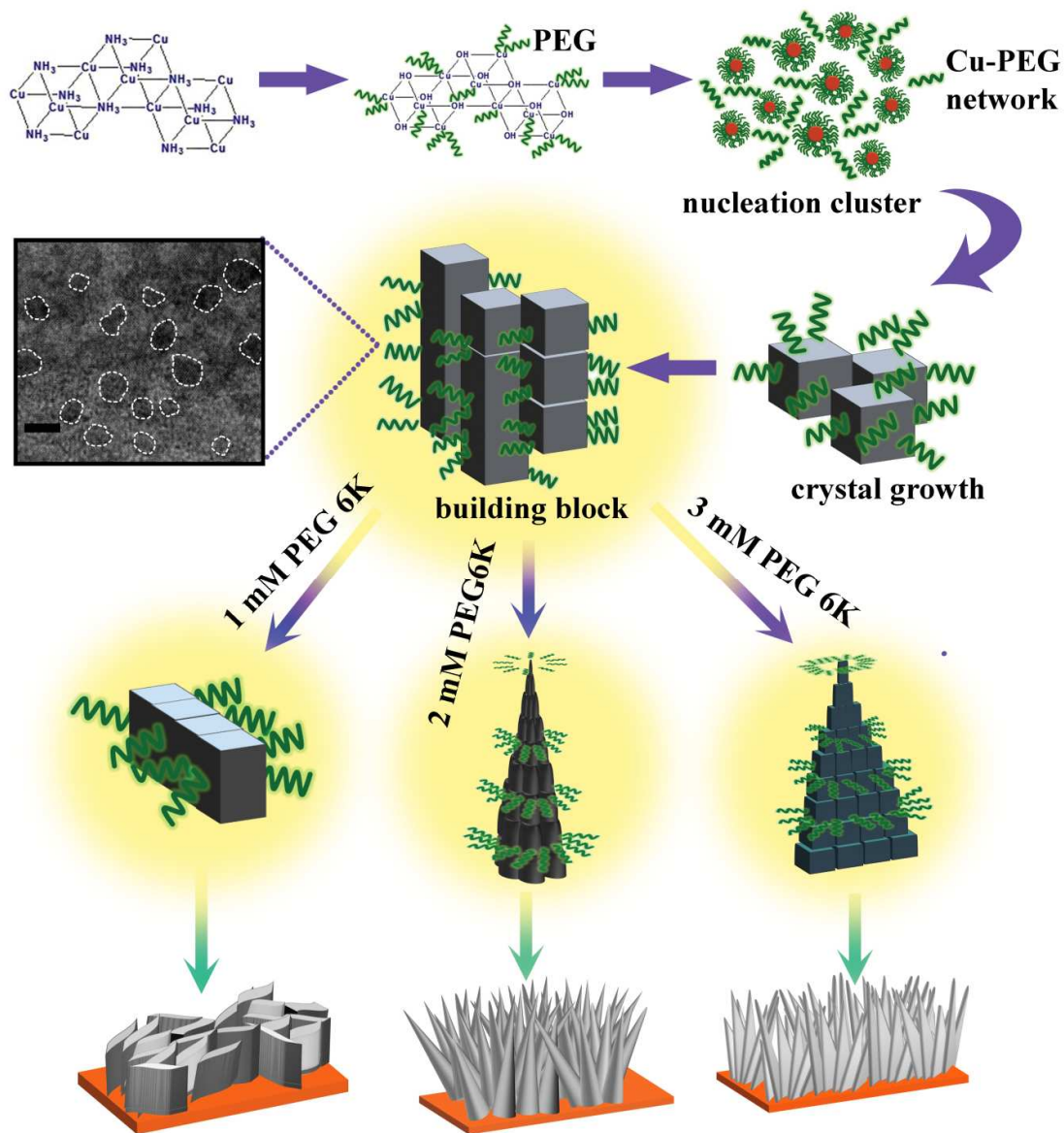


Fig. 4

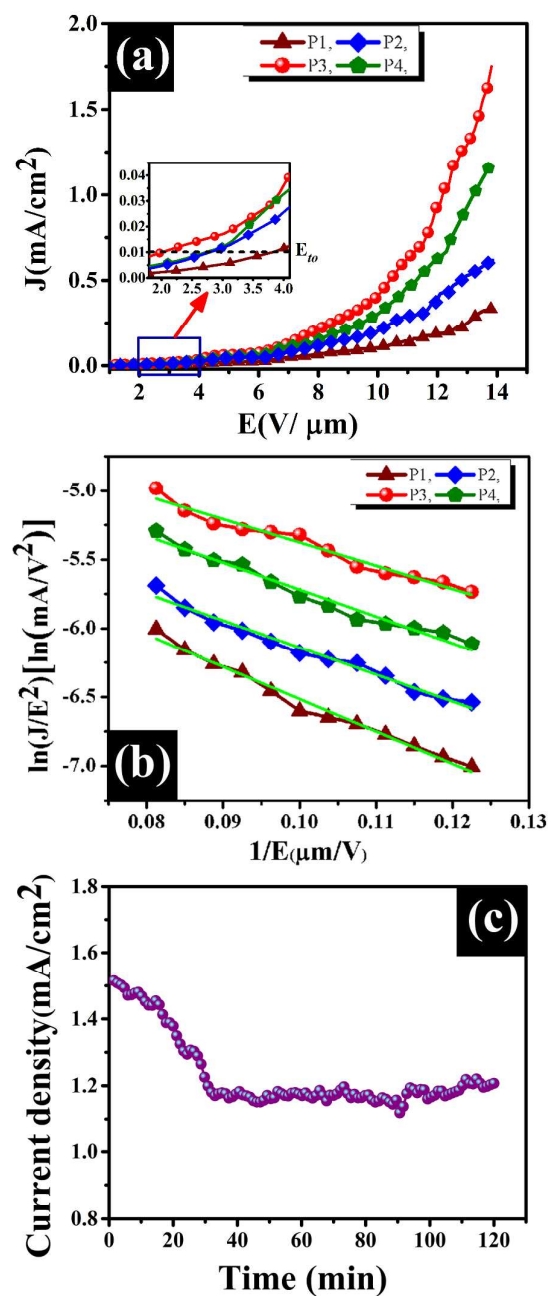


Fig. 5

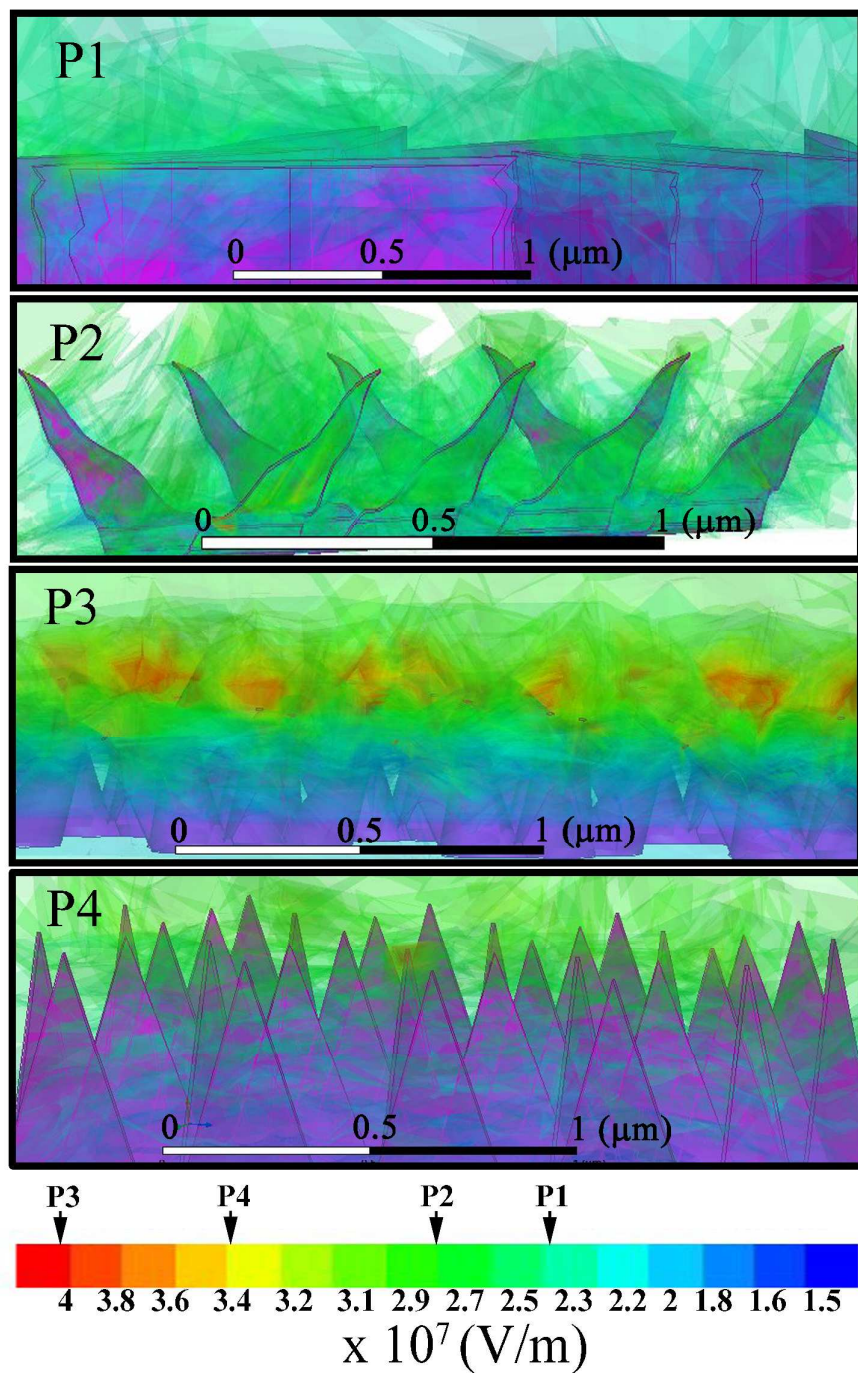


Fig. 6

†Electronic Supplementary Information (ESI):

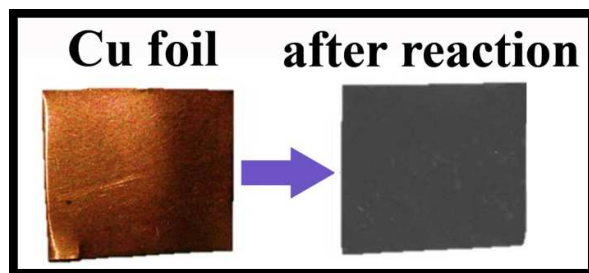


Fig. S1 showing the optical image of the copper film before the reaction and after synthesis, the Cu foil turned uniformly black, which evidences a uniform deposition of CuO all over the substrates surface.

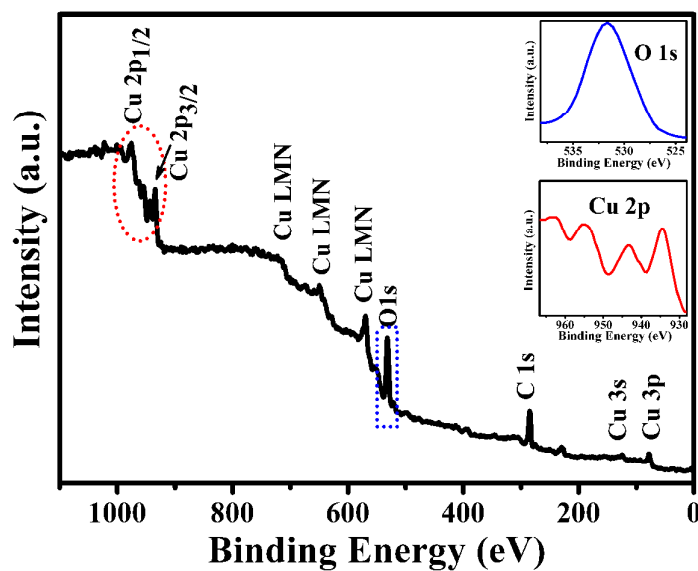


Fig. S2 shows the XPS survey spectra of samples P3. The peaks corresponding to Cu 3d, 3p, 3s, 2p and Auger, O 1s and Auger are obviously observed. Survey spectra strongly discard any possibility regarding the presence of impurity agents in the synthesized nanostructures.

Furthermore, the selected core level peaks of Cu 2p and O 1s has been magnified in the inset of the survey spectrum.

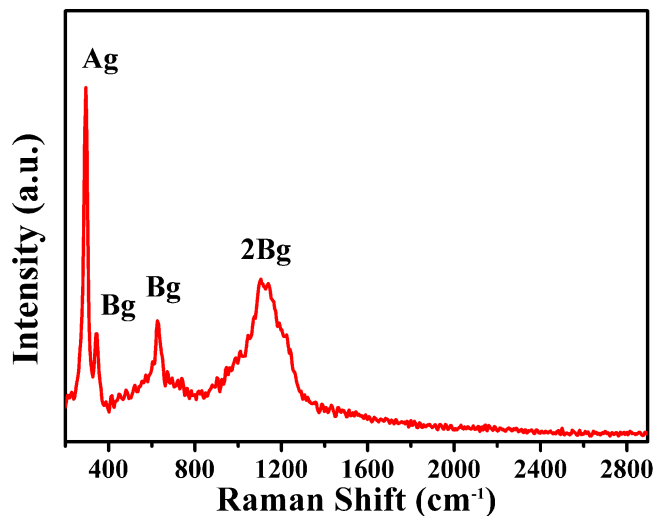


Fig. S3 shows the Raman spectra of the CuO nanostructures for the entire range of 200 – 2900 cm⁻¹. The spectrum does not show appearance of any Raman modes of Carbon (D=1363 and G=1593 cm⁻¹) in entire scan range which scientifically admits no appearance of carbon/ carbonate during synthesis of CuO nanostructure. Moreover the spectrum clearly specifies the uniform growth of CuO nanostructures over the entire substrate (Cu foil).

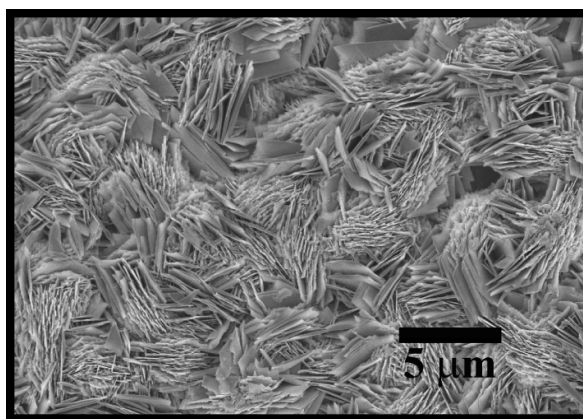


Fig. S3 showing flake like morphology of CuO without any structure regulating agent.

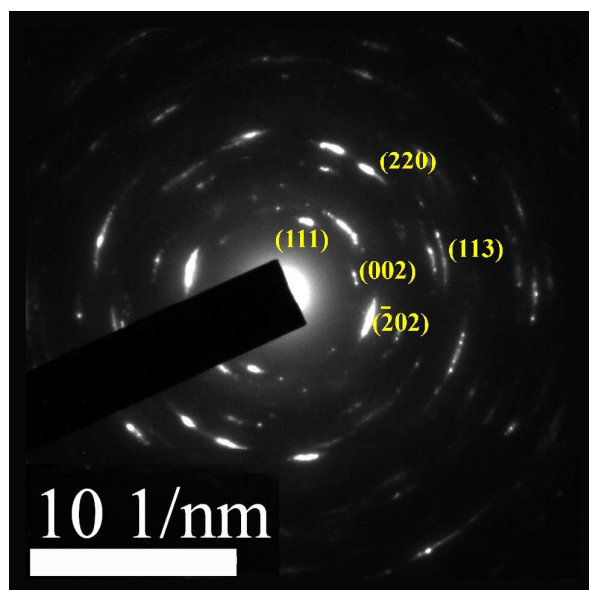
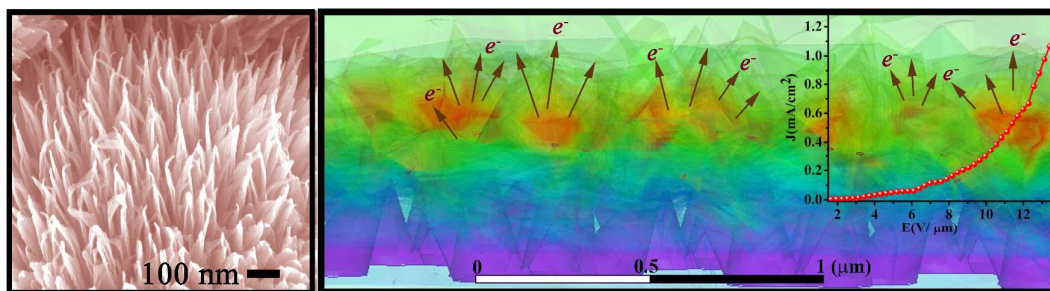


Fig. S4 is showing the typical SAED pattern of individual nanoneedle (sample P3) of CuO nanostructures

Table of Content (TOC):

Wet chemically developed CuO nanoneedles show lower turn on value along with heightened enhancement factor. Structural anisotropy mediated better field enhancement characteristics is also reflected from the simulated data.